

Quiet Sun EUV transient brightenings and turbulence

A panoramic view by EIT on board SOHO

D. Berghmans¹, F. Clette¹, and D. Moses²

¹ Royal Observatory of Belgium, Ringlaan 3, B-1180 Brussel, Belgium

² Naval Research Laboratory Code 7660.1, 4555 Overlook Ave Washington, DC 20375, USA

Received 2 March 1998 / Accepted 25 May 1998

Abstract. Since January 1996, the Extreme-Ultraviolet Imaging Telescope (EIT, onboard SOHO) has produced unique image sequences covering a wide field of view with a high temporal resolution, in the He II transition region line and in several Fe coronal emission lines. Using two sequences acquired with cadences of the order of one minute and with durations ranging from one hour to several hours, we analyse the dynamical properties of the transition region and corona. We find evidence of turbulence both in spatial and in temporal power spectra suggesting that the plasma of the quiet solar atmosphere is in a permanent state of turbulence.

As predicted by numerical simulations, this turbulence has an highly intermittent nature. We find an unexpectedly large number of small-scale brightenings. The coronal brightenings are identified as the low energy counterparts of “X-ray network flares” observed with SXT on board Yohkoh. The thousands of brightenings observed by EIT in the transition region include many that are similar to “blinkers” observed with CDS, though we find a larger variety.

Thanks to EIT’s wide spatial coverage, we can perform a large scale statistical study, complementing spectroscopic studies which give access to only a very small subsample of events. We present occurrence distributions of duration, size and radiative output of the brightenings as well as various correlations between these parameters. The energy injected by the brightenings into the solar atmosphere is insufficient to be in itself responsible for coronal heating. We discuss the importance of the ubiquitous small brightenings as perhaps the most visible aspect of yet undetected heating events higher up in the quiet corona.

Key words: Sun: corona – Sun: transition region – Sun: UV radiation – turbulence

1. Introduction

Only five years ago, Rabin & Dowdy (1992) asserted that: “The more carefully we look for the quiet Sun, the harder it is to find”. With the advent of the Solar and Heliospheric Observatory

(SOHO, launched December 1995), this statement has become prophetic. Whereas the quiet solar atmosphere was traditionally depicted as an assembly of large-scale magnetic structures that emerge from the photosphere and fan out in the corona, the SOHO instruments now reveal a finely structured medium constantly agitated by a wide variety of transients (e.g. Innes et al. 1997; Harrison 1997a, 1997b). This remarkable variability brings the possibility of discriminating between various coronal heating processes.

All the proposed heating mechanisms share common ground. According to Alfvén’s frozen flux theorem, footpoints of the magnetic field lines are forced to follow the convective motions of the photospheric plasma. By this process, the kinetic energy of the convective motions is converted into magnetic energy, which in turn might be converted into heat higher up in the atmosphere. Taking into account the enormous value of its Reynolds number, it is clear that the corona must be in a turbulent regime. This brought Hollweg (1983) to suggest that the kinetic energy injected over large scales by sub-photospheric convective motions might cascade down through non-linear interactions to sufficiently small scales for viscosity and resistivity to produce an efficient dissipation.

In Fourier space, this wide scale range leads to a broad-band power spectrum, traditionally divided in an energy containing region at low wavenumbers, where energy is injected and a dissipation region at high wavenumbers. In between is the inertial region where nonlinear interactions dominate. This region is characterised by the *power law index*, which was first derived by Kolmogorov (1941) for the hydrodynamic case ($-5/3$) and later by Kraichnan (1965) for the magnetohydrodynamic (MHD) case ($-3/2$). More advanced models of MHD turbulence (Grappin et al. 1983) show that this latter value might decrease down to -3 for an increasing correlation between the velocity and magnetic field fluctuations.

Given the difficulty of the problem, only a few analytical models of MHD turbulence were developed in the context of coronal heating (Gómez 1990; Heyvaerts & Priest 1992; Gómez et al. 1993b). A more promising approach seems to be that of numerical simulations, which show that for large Reynolds numbers, MHD turbulence has an highly intermittent nature (Einaudi et al. 1996). The associated discrete releases of energy corre-

spond to forced reconnection in localised current sheets (Georgoulis et al. 1997). They have been called either microflares or nanoflares depending on their energy content with respect to the largest active region flares (Parker 1988; Parker 1991). Weak transients have indeed been observed, but mostly in active regions and with energies in the upper microflare range (e.g. Porter et al. 1984, 1995; Shimizu 1995; Shimizu & Tsuneta 1997). At transition region temperatures, a very large number of “EUV explosive events” have been detected (Brueckner & Bartoe 1983) and it has been suggested recently that they are reconnection sites with associated bi-directional plasma jets (Innes et al. 1997).

Some recent studies revealed the existence of quiet Sun coronal and transition region transients, called network flares (Krucker et al. 1997b) and blinkers (Harrison 1997a, 1997b) respectively. Small-scale, inner corona reconnection events have gained new interest since Schrijver et al. (1997) suggested that these events might braid the footpoints of coronal magnetic field lines more efficiently than photospheric granulation. Until now however, only a handful of these transients have been studied, over very small areas and limited durations. Thus, several of their properties are poorly known, for example the occurrence rate, the diversity of time profiles, the time-evolution of the spatial extent and the global spatial distribution. In particular, the energy distribution of these events provides a fundamental diagnostic for the adoption of the nanoflare mechanism as a viable coronal heating process. Indeed, if small energy events sufficiently outnumber the larger events, enough energy would be contained in the smallest events, below the detection limit to sustain a persistent, hot corona (Hudson 1991).

In this paper, we analyse two image sequences of the quiet Sun, acquired by the EIT in the He II transition region line and in the Fe XII coronal line. We interpret the observed EUV intensity fluctuations as the observable manifestation of turbulent velocity fields and associated cascading energy releases. Although the temporal (1 min) and spatial resolution (3.75 Mm) is limited, EIT’s wide field of view offers the unique possibility of deriving reliable statistical properties from the large population of variable EUV sources. The extensive temporal and spatial coverage offered by EIT complements spectroscopic studies, which only give access to very small subsamples of these very numerous events.

The paper is organized as follows: In Sect. 2, we discuss the image pre-processing. In the following section, we present spatial (Sect. 3.1) and temporal (Sect. 3.2) Fourier transforms of the image sequences. Some of the resulting power spectra show clear power law profiles, which are interpreted in terms of turbulence theory. Since power spectra of local features (Sect. 3.3) show evidence of transient behaviour, Sect. 4 is devoted to the search for transient intensity enhancements. In Sect. 4.1., we present the detection method that allowed us to detect innumerable EUV brightenings in the transition region (Sect. 4.2) and in the corona (Sect. 4.3). We derive global statistical properties of these events, and investigate how those “quiet Sun brightenings” can be related to other classes of transients studied before and with the “magnetic carpet” concept. Finally, we try to esti-

Table 1. General characteristics of the image sequences taken in the He II transition region line and in the Fe XII coronal line on December 28, 1996.

Sequence	He II	Fe XII
wavelength	304 Å	195 Å
peak formation temperature	8.0×10^4 K	1.6×10^6 K
begin time	16h10m21s	20h53m26s
end time	19h20m56s	21h59m08s
total duration	3h10m35s	1h05m42s
number of images	173	55
average sampling time	66.483 s	70.516 s

mate the amount of energy carried by these quiet Sun transients in order to derive the global thermal energy input associated with them. To conclude, Sect. 5 summarizes and discusses our main results.

2. Description of the data

2.1. Pre-processing procedure

On December 28, 1996, the EIT instrument (Delaboudinière et al. 1995) observed a square area (600 Mm x 600 Mm) in the central part of the solar disc for about 3 hours in the He II transition region line and 1 hour in the Fe XII coronal line. Images were sampled once a minute on average for both sequences (unequal sampling). Data characteristics are summarized in Table 1.

The raw 320×320 pixel images were first corrected for various cosmetic defects (flat-field and grid pattern corrections). In the following step we took care of the noise produced by variations in the exposure time due to small random fluctuations of the shutter closing time. Although these small variations of the exposure time are temporally random (Poisson statistics, 0.4 s rms), they affect the whole field of view by the same quasi-uniform factor. As a consequence, this noise source is the most difficult to compensate for, since it will not be statistically reduced by spatial averaging (in contrast with the photon shot noise). By rescaling the integrated intensity in individual images to the full-sequence average, we could reduce this noise component below 0.7% and 0.4% rms, in the He II and in the Fe XII sequence respectively.

Pixels recording cosmic rays or belonging to missing data blocks were identified, and their values were restored by linear interpolation between the neighbouring images. The detection of cosmic rays was implemented by computing the average signal level and the standard deviation σ over 5 images and then by identifying single pixels or linear streaks that exceeded the 5σ level above average, thus taking advantage of the limited changes between successive images and the fact that cosmic rays appear in single images. This method was carefully tuned in order to achieve an almost complete rejection of cosmic ray hits without interfering with our subsequent search for micro-

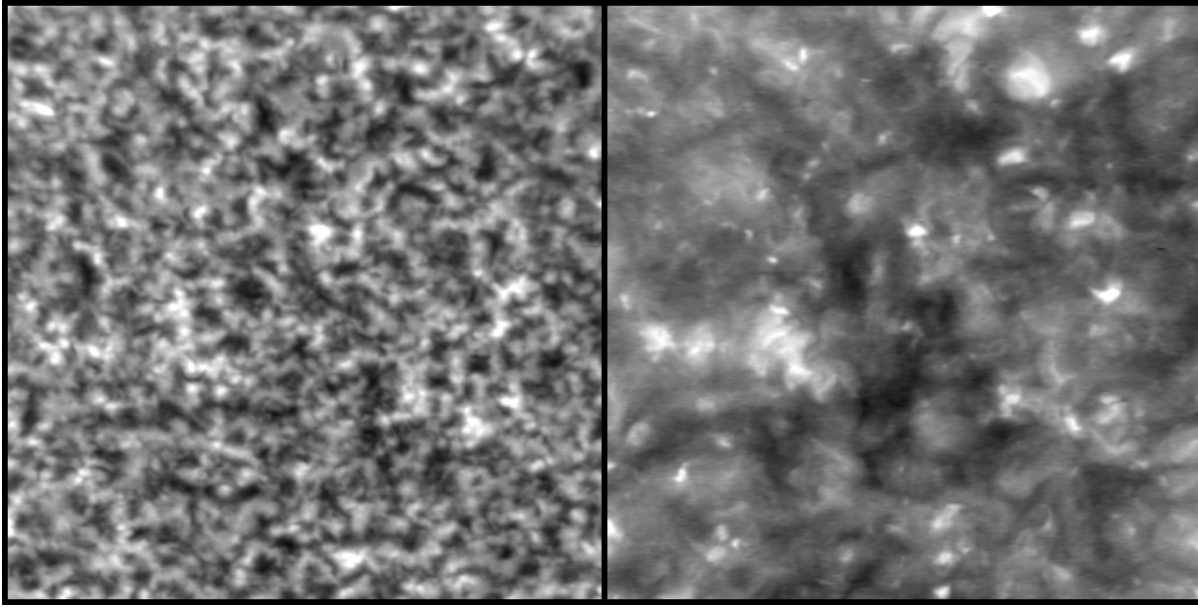


Fig. 1. Average intensities in corrected and projected images of the He II (left) and the Fe XII image sequence (right).

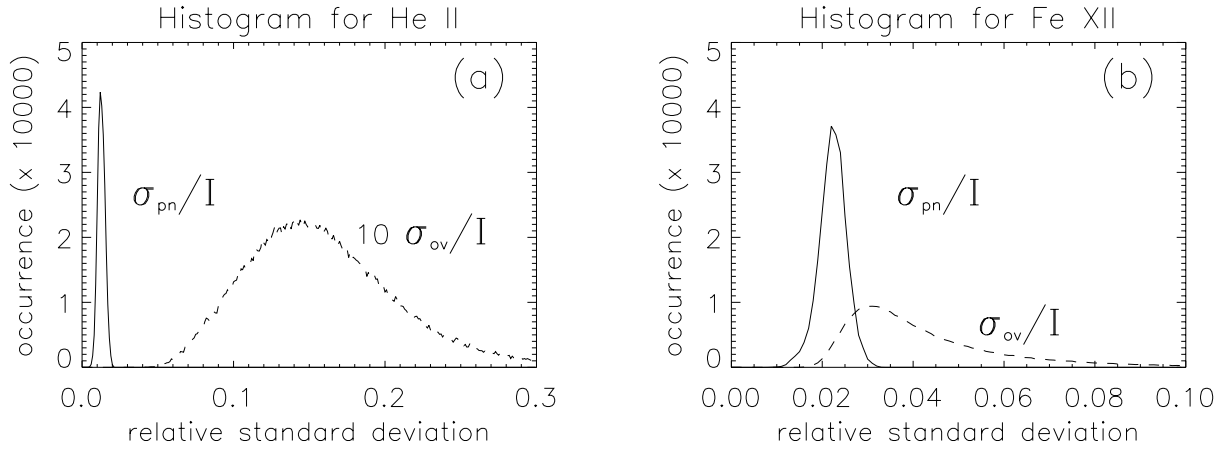


Fig. 2a and b. Histograms for the He II sequence (a) and the Fe XII sequence (b) showing the distribution of the instrumental noise (solid line) and of the observed fractional variability (dashed line).

variability. The detected cosmic ray flux amounts to about 150 counts per minute of integration over our subfield, which translates into a rate of $375 \text{ min}^{-1} \text{ cm}^{-2}$ at EIT's focal plane.

Finally, in order to compensate for projection effects and solar differential rotation, we interpolated the corrected images onto a regular grid in heliographic coordinates, using bilinear interpolation. We chose a grid step of 6 arcmin, or 1.2 Mm, in longitude and latitude, while the intrinsic resolution of the instrument is of the order of 3.75 Mm.

2.2. Global statistical properties

Structures in the average intensity maps (Fig. 1) look sharp despite the long time integration, which indicates that the large-scale structures making up the quiet corona and transition region network are stable over timescales as long as 3 hours. On the

other hand, when small scales are considered, variability is seen everywhere. In Fig. 2a and b, we show histograms of the standard deviation of the fractional fluctuations relative to the average pixel intensity (σ_{ov}/I , dashed line) for the transition region sequence (Fig. 2a) and for the coronal sequence (Fig. 2b). As a comparison, the solid curve represents the distribution of instrumental noise, which is mainly due to the photon shot noise. The corresponding standard deviation σ_{pn} is given by the empirical formula:

$$\begin{aligned} \sigma_{pn} &= \sqrt{0.18 I + 2.7} && \text{for He II and,} \\ &= \sqrt{0.25 I + 2.7} && \text{for Fe XII,} \end{aligned} \quad (1)$$

where the detected intensity I and the standard deviation σ_{pn} are expressed in DN units.

Over the whole field of view, the fractional variability σ_{ov}/I equals 16% in the He II line and 5% in the Fe XII line on aver-

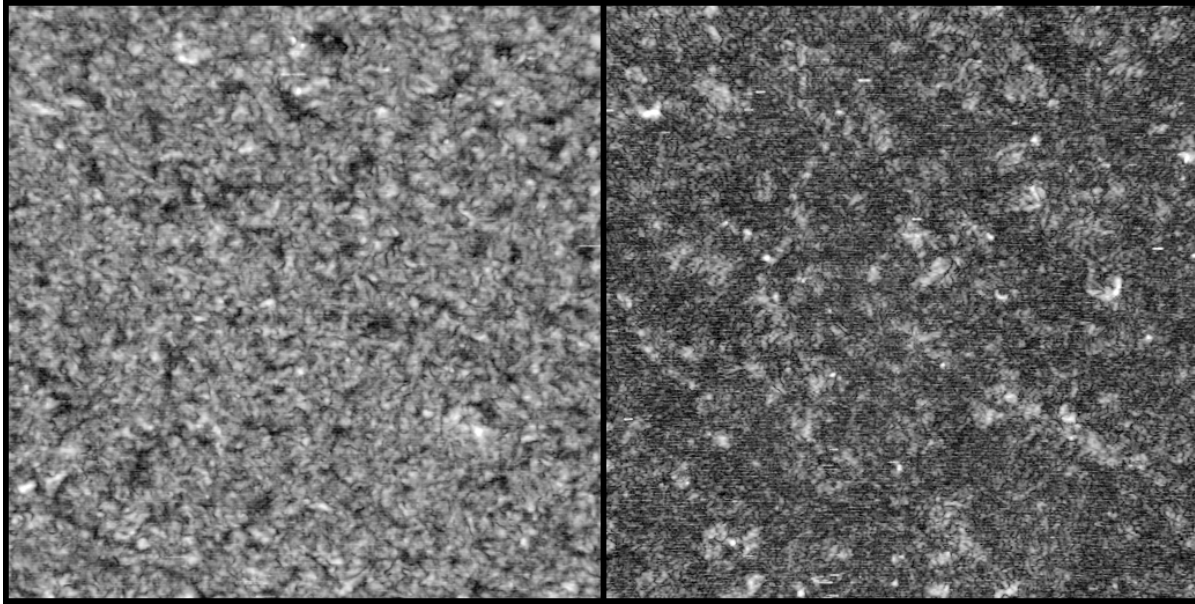


Fig. 3. Maps of the local standard deviations over the He II (left) and Fe XII (right) fields-of-view. The scale and orientation are identical to those of Fig. 1.

age. It reaches extremes of 77 % and 57 % in the He II and Fe XII line respectively. A comparison between the observed variability σ_{ov}/I and the photon shot noise variability σ_{pn}/I reveals a fundamental difference between both sequences.

In the coronal sequence (Fig. 2b), the main distribution of the observed variability is just slightly higher than the instrumental noise. Still, the main distribution is extended by a subpopulation of pixels with variabilities significantly larger than the instrumental noise, so that on average $\sigma_{ov} \sim 2.0 \sigma_{pn}$. The fraction of the intrinsically variable pixels can be estimated at about 77 %.

On the other hand, in the transition region sequence (Fig. 2a), the ratio of the observed standard deviation with the instrumental noise is much larger and ranges typically from 3 to 18, with an average of 12.4. Obviously, every pixel in the field of view shows significant intrinsic variability in the He II line, in agreement with earlier results derived from other transition region emission lines (Rabin & Dowdy 1992).

The spatial distribution of the relative EUV variability, illustrated for both spectral lines in Fig. 3, displays much finer structures than the average intensity distribution (Fig. 1). Although variability patterns loosely trace the magnetic network, there is no one-to-one correspondence between strongly variable features and the local EUV intensity. In the coronal sequence, only a few loops and bright points show a strong variability, while others were apparently quiescent for the duration of the observations. In agreement with the histogram Fig. 2a, significant variability is found over the whole surface of the transition region.

3. Power spectra

3.1. Spatial power spectra

In order to study spatial properties, we submitted each individual image to a two-dimensional spatial Fourier transform. Although details in the spatial spectra vary with time due to small intrinsic solar changes and to instrumental noise, we found that the overall power distribution $P_i(k_x, k_y)$ of the individual spectra is constant over the duration of the observations. So, statistically, the ensemble properties of the system are time-invariant, and we can compute the average of all power spectra $\langle P_i(k_x, k_y) \rangle$, further decreasing the noise contribution. In both wavelengths, we find a broadband isotropic power spectrum (Fig. 4). Such a distribution, in which energy is spread over a wide range of wavenumbers, can be interpreted as the signature of stochastic or chaotic dynamics. Given the azimuthal symmetry of the spectrum, we then constructed the omnidirectional power spectrum by integrating over the polar angle θ :

$$P(k) = k \int_0^{2\pi} d\theta \langle P_i(k \cos \theta, k \sin \theta) \rangle, \quad (2)$$

as specified by Gómez et al. (1993a).

In the Fe XII coronal line, this omnidirectional spectrum (Fig. 5) has a power law distribution with an index of -2.52 ± 0.05 for wavenumbers $k < 1.8$ rad/Mm. Above this wavenumber, it is affected by the modulation transfer function of the instrument and aliasing. This index value falls within the 2.5–2.6 range derived by Martens & Gómez (1992) from NIXT and YOHKOH/SXT observations of active regions. The -2.7 index value found by Benz et al. (1997) for a YOHKOH/SXT subfield image of the quiet disc corona at temperatures of several million K, is slightly higher, but this difference is probably not significant (the accuracy is not given by these authors). In a model that

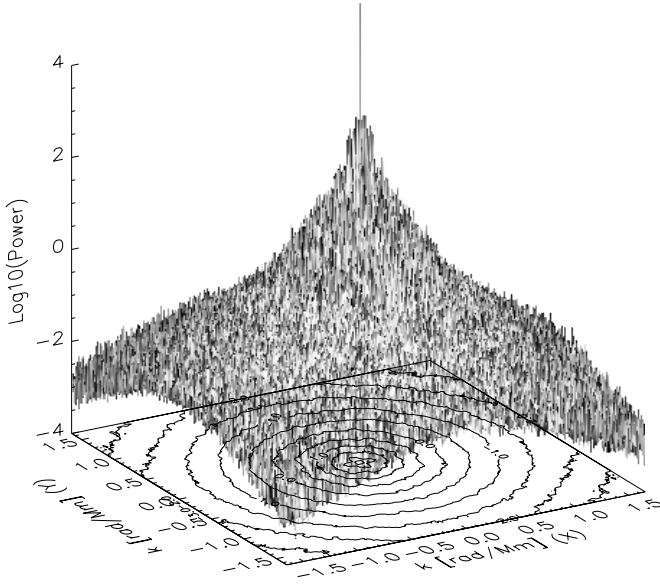


Fig. 4. Two dimensional temporally averaged spatial power spectrum $\langle P_i \rangle$ of the He II images as a function of k_x and k_y .

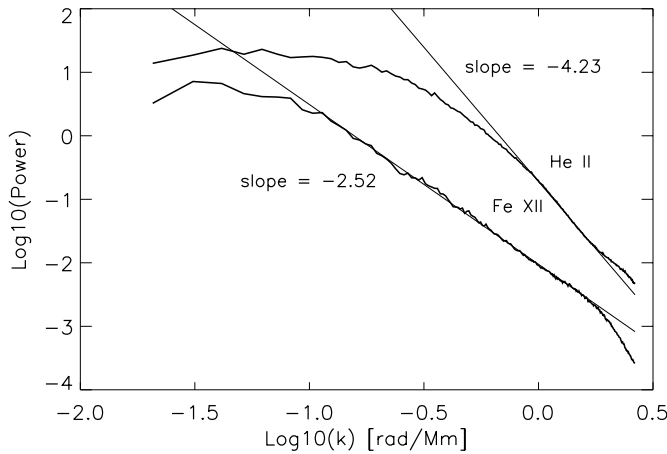


Fig. 5. Omnidirectional spatial power spectra $P(k)$ of He II transition region and Fe XII coronal images.

relates the coronal magnetic fluctuations to the subphotospheric hydrodynamic turbulence, Gómez et al. (1993b) find a higher index value of -3. However, they also mention that including observations of the photospheric velocity field yields a power law index of -2.2. By adjusting slightly the spectral distribution of the energy source, this model might thus reproduce the spatial power spectra of soft-X ray and EUV emissions. More recently, a 2-dimensional MHD simulation of plasma turbulence induced by photospheric eddies in a loop shows the formation of energy dissipation patterns with a spatial scaling index of -2.6 ± 0.2 (Georgoulis et al. 1997). Although this value might increase as the spatial resolution of the model is increased, it again confirms the high index value derived from our EIT coronal images.

In YOHKOH/SXT power spectra derived by Benz et al. (1997), a break point seems to be located at 0.27 rad/Mm, which

corresponds to a scale of 23 Mm, i.e. slightly less than the supergranulation scale. In our spectra, this break point is displaced towards lower wavenumbers, below 0.13 rad/Mm, which corresponds to a larger scale of ≈ 50 Mm. Considering the fact that the resolution of the SXT spectrum is limited at small wavenumbers by the smaller field-of-view, this discrepancy indicates that this 0.27 rad/Mm break point is of instrumental origin. However, whether the power law spectrum really breaks at ≈ 50 Mm, i.e. at the supergranulation scale, as found here is still uncertain.

In contrast, the He II omnidirectional spectrum (Fig. 5) cannot be fitted by a single power law distribution. The power distribution is almost flat below 0.2 rad/Mm. The slope then increases steadily and reaches a maximum of -4.2 above 1 rad/Mm. In fact, the general shape of this transition region spectrum becomes similar to the power spectrum of solar granulation (see Chou et al. 1991). However, the power law index for photospheric granulation stays below -2.7, and in our transition region spectrum, there is no clear break-point at 1 rad/Mm, which corresponds to the mesogranulation scale (≈ 6000 km). Compared with the coronal spatial spectrum, this distribution hints at a different turbulent regime, where an energy excess is injected at high wavenumbers (smallest spatial scales) by some mechanism that becomes progressively less efficient above the supergranulation scale (average network mesh size). This mechanism is apparently associated with a large number of fairly localised features, that can be identified as the quasi-static bright network elements but also as the uniformly distributed brightenings which animate the whole transition region, as described in Sect. 4.

Our new results thus confirm that the spatial distribution of EUV coronal emission supports the concept of an MHD turbulent energy cascade, both in the corona and in the transition region. Moreover, as the narrow temperature sensitivity of the EIT 195 Å bandpass peaks at 1.5×10^6 K, we provide the first evidence that the same dynamical regime is found in the cool plasma structures of the quiet corona (weak and small-scale magnetic fields) as in the active region loop systems (strong fields, extended loops). Finally, the observed departure from a power law at low wavenumbers probably reflects the scale-distribution of the underlying energy source and suggests that a transition occurs around the supergranulation scale in the transition region and maybe at a slightly larger scale in the corona.

3.2. Temporal power spectra

After an initial preprocessing (conversion to fractional deviations, average correction, apodisation by a 5% cosine taper), the normalized images were submitted to a one-dimensional discrete Fourier transform for unequally spaced data (Deeming 1975) along the time dimension. In order to improve the signal-to-noise ratio in the power spectra and to simultaneously study the local variations of the temporal power spectra, we defined different classes of objects and computed the average power spectrum for the pixels contained in every local structure belonging to those classes. In the coronal images, we distinguished the following classes of structures, in increasing order of brightness:

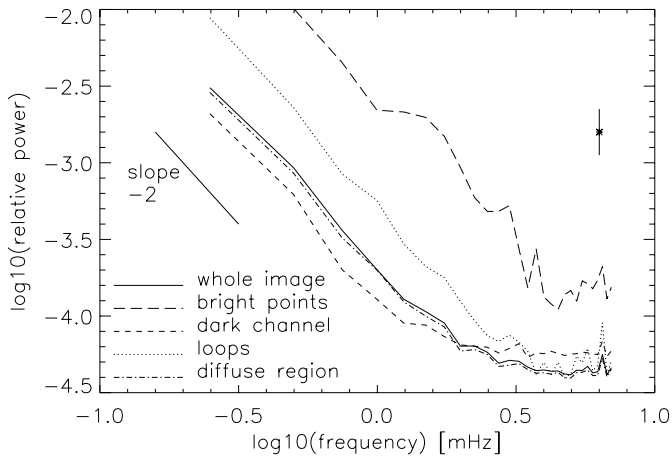


Fig. 6. Average power spectra of different classes of coronal structures, compared with the global power spectrum. The vertical bar indicates the estimated error (For the bright point spectrum this error is about 3 times larger).

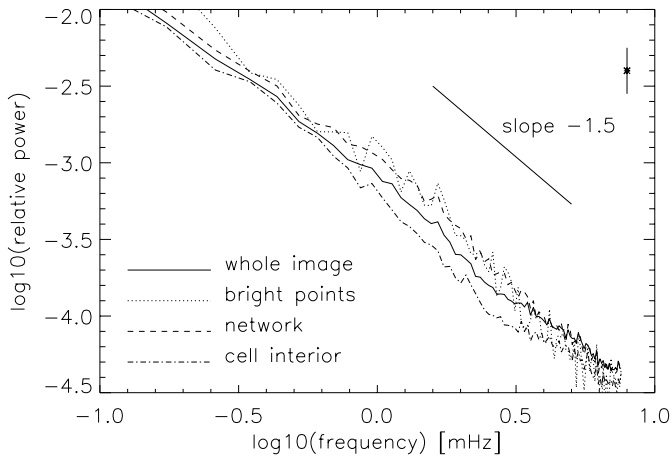


Fig. 7. Average power spectra of different classes of transition region structures, compared with the global power spectrum. The vertical bar indicates the estimated error. (For the bright point spectrum this error is about 3 times larger)

- dark channels, which look like small open-field regions similar to coronal holes,
- the diffuse background corona, an intricate texture of dim loops which form the so-called “magnetic carpet”,
- bright loop structures (resolved morphology),
- bright points (unresolved compact sources).

The distinction between the last two classes is often ambiguous, because many bright points show some structure at EIT’s resolution and might even be local “hot-spots” of faint loops. As the transition region network has a more random character, we separated only the darkest cell-centers (inter-network) from the network itself, and also some of the brightest elements, like bright points, by simple thresholding. For both sequences we selected visually a few thousand pixels for each class, except for the bright point classes which consist of only a few hundred pixels.

Table 2. Power law indices for different classes of structures in the quiet corona.

Object class	Average index
Bright points	-1.99 ± 0.13
Loops	-2.06 ± 0.05
Background	-1.93 ± 0.05
Dark lanes	-1.62 ± 0.04
Whole image	-1.85 ± 0.10

Table 3. Power law indices for different classes of structures in the transition region.

Object class	Average index
Bright points	-1.50 ± 0.10
Network	-1.40 ± 0.06
Inter-network	-1.55 ± 0.05
Whole image	-1.50 ± 0.10

Power spectra (square of fractional amplitudes) averaged over all coronal objects belonging to the above classes are plotted in Fig. 6. All spectra share the same power law distribution, except for dim regions where the power levels off at high frequencies due the instrumental noise. They differ by a uniform power ratio, with a maximum of 20 in relative power between bright points and the darkest hole-like regions. However, the relative power stays fairly constant over most of the solar surface, i.e. the amplitudes of the fluctuations are simply proportional to the average local EUV emission. A significant power excess is observed only inside bright points. The power law index stays remarkably constant, at about -2 , for the diffuse background, loops and bright points (Table 2). The index for dark lanes is slightly lower (-1.62), but this value may be underestimated due to the larger instrumental noise at high frequencies. Averaging the power spectra over the whole field of view results in an intermediate index of -1.85 ± 0.1 . Those general properties are in good agreement with the results derived from another EIT data set by Krucker et al. (1997a).

Fig. 7 and Table 3 provide the same comparison for transition region structures. Here again, the power increases steadily from dark network centers to the brightest network elements, but by a much smaller amount. The average spectra of bright points and of the rest of the network are almost indistinguishable. However, over a broad range of frequencies (0.5–4 mHz), the network presents a slight power excess relative to the inter-network elements (ratio ≈ 2) (see Fig. 8). This corresponds to a 1.4 increase in relative amplitude, whereas the intensity ratio amounts to about 5. The power law index shows no significant variation, as was the case in the corona.

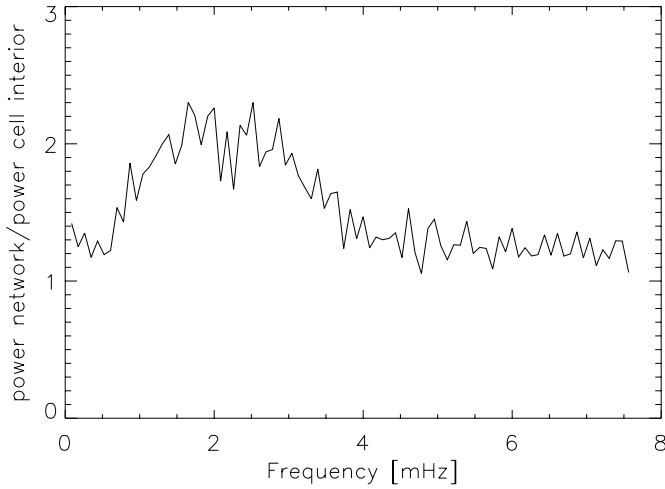


Fig. 8. The ratio of the power of transition region structures in the network to the power in cell interiors versus frequency. The ratio of the power in bright points to the power in cell interiors is very similar.

Just like the 2-dimensional spatial power spectra, all the above temporal spectra follow a power law distribution, again providing evidence for a turbulent energy cascade. However, the index values for the temporal variability are lower. The power law index of -1.50 ± 0.1 , found for the He II line, comes very close to the $-3/2$ index suggested by Kraichnan (1965) for an MHD turbulent spectrum. We thus speculate that frequencies in the range 0.1–7.5 mHz fall within the inertial range of MHD turbulence. In the Fe XII line, the spectrum is significantly steeper (-1.85 ± 0.1). Although this slope remains compatible with a the $-3/2$ index, it is closer to $-5/3$ value of the *Kolmogorov* spectrum (Kolmogorov 1941). This association suggests a system of fully developed turbulence, with energy being injected and dissipated on timescales outside the range accessible in our spectra. The observed power distributions remain almost constant over a wide range of local plasma states, from the dark cell interiors to the bright cell boundaries in the transition region network, or from dim loop patterns up to bright points in the corona. We can thus infer that most elements in the quiet corona share the same dynamical regime and that the same basic physical mechanisms seem to be at work over the whole transition region. In particular, the He II fractional variability in cell interiors is not negligible, as it is only slightly lower than on the cell boundaries, despite the difference in magnetic field strength and configuration.

No significant local power excess is found in either global spectrum, in particular within the 5-min and 3-min period ranges of photospheric and chromospheric oscillations. Such coherent oscillations are thus either fully reflected or strongly attenuated at the base of the corona, with residual amplitudes below our detection level (0.4% in relative amplitude). However, waves that are excited or propagate locally within small-scale magnetic structures are not excluded, but they could escape detection in a global statistical average. On the other hand, coronal bright points display a significant broad-band power excess and seem to be heated at least partly by a different mechanism. This assumption is confirmed by considering typical differen-

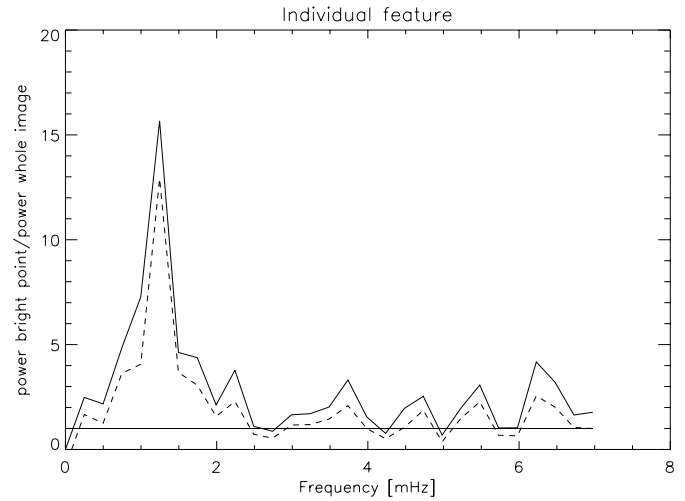


Fig. 9. Sample power spectrum of an individual coronal bright point, scaled by the power of the whole image. One or more peaks are typical in the range 0.5 to 2 mHz. The dashed line corresponds to the $2.5 \sigma_{pn}$ significance level.

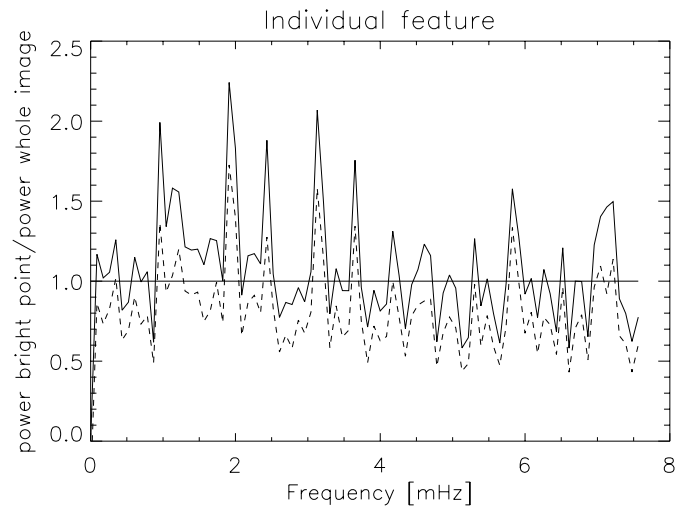


Fig. 10. Sample power spectrum of an individual bright point in the transition region, scaled by the power spectrum of the whole image. The dashed line corresponds to the $2.5 \sigma_{pn}$ significance level.

tial power spectra of individual bright points in the transition region (Fig. 10) and in the corona (Fig. 9). These differential power spectra, obtained by scaling the local spectrum relative to the power spectrum of the whole image, always contain one or several discrete peaks in the frequency range 0.5–4 mHz, which might be the signature of wave heating or intermittency (Schuster 1984). Such discrete spectral features are absent from the broadband spectra of the other regions. When summing spectra of many individual features, these power peaks accumulate and are responsible for the broadband excess seen in the transition region network (Fig. 8).

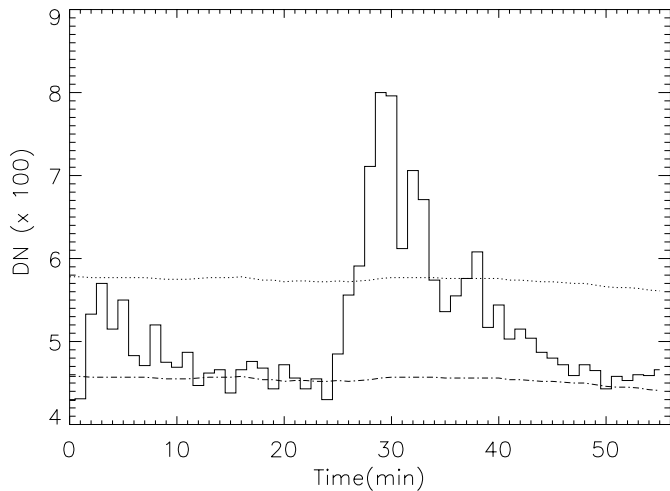


Fig. 11. Example of a light curve (solid line) of a single pixel in the coronal sequence showing a brightening. As a reference we also provide the calculated -see Sect. 4.1- background intensity (dot-dashed line) and the $\Sigma_P = 3 \sigma_{ov}$ level (detection limit, dotted line).

4. Impulsive brightenings

The presence of multiple peaks scattered randomly over a broad frequency range can be interpreted as the signature of intermittency. This means that sharp transitions, occurring randomly in time, are expected to be present in individual light curves. A visual inspection of the light curves (see Fig. 11 and Fig. 12) of a few regions displaying such peaks in their power spectrum indeed reveals transient intensity enhancements. This kind of dynamical behaviour fits the prediction of transients and random energy injections by local reconnection (nanoflare theory) and therefore merits special attention. By browsing through the data, we found that these brightenings happen frequently enough over our wide field of view to require an automated detection scheme. Since the criteria used in any detection method may lead to selection effects and therefore introduce biases in the statistical properties, we will first describe our detection method in full detail.

4.1. The brightening detection scheme

Variations in intensity measured over one or more EIT pixels can be attributed to different causes. First of all, the large-scale structure of the solar atmosphere is evolving slowly, introducing slow trends in the background emission. Superimposed on this local background, we are looking for “brightenings” i.e. both temporally and spatially localised emission enhancements. The detection of such brightenings is hampered by several random components in the images that produce variations in the same scale range, namely: photon shot noise, exposure time fluctuations and overlooked cosmic rays. We used the following automated detection scheme to distinguish between random noise variations and genuine solar brightenings:

1. *Defining a reference background emission.* Starting from the pre-processed image sequence, we construct a “back-

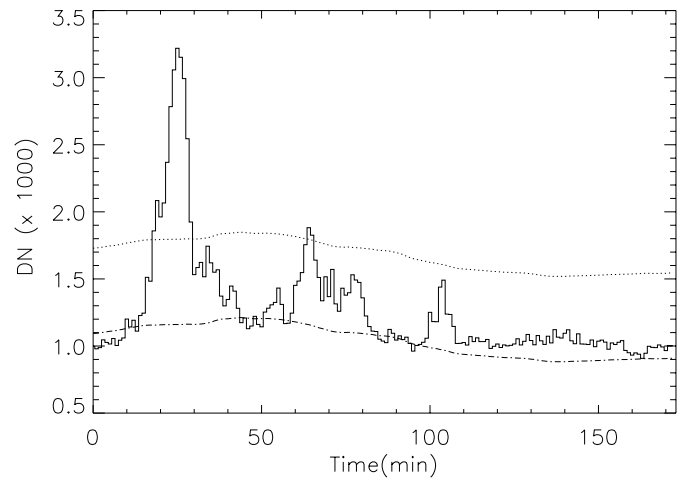


Fig. 12. Example of a light curve (solid line) of a single pixel in the transition region sequence. This somewhat special pixel was selected for the succession of a large brightening ($t = 25$ min), a more average brightening ($t = 65$ min), a small brightening that escaped detection ($t = 105$ min) and small variability in agreement with the expected photon shot noise ($t = 140$ min). As a reference we also provide the calculated -see Sect. 4.1- background intensity (dot-dashed line) and the $\Sigma_P = 3 \sigma_{ov}$ level (detection limit, dotted line).

ground emission” sequence in two successive steps. First, we compute a running average of the light curve of each pixel over a time-window of 1 hour for the He II sequence and 30 min for the Fe XII sequence. Although this removes most of the high frequency temporal variations, strong and slowly decaying brightenings often leave broad artificial enhancements in the resulting smoothed sequence. These artifacts can be suppressed further by taking into account the temporal evolution of neighbouring pixels. This is achieved in a second step through a spatial “boxcar” smoothing over a 5×5 pixel neighbourhood. However, since we do not want to smear out spatial structures, each light curve is scaled to unity prior to spatial smoothing, and rescaled again to its original average level after the spatial smoothing. The result is a smooth background sequence which can be used as a good approximation of a steady-state “quiet” emission level (see Fig. 11 and Fig. 12). In addition, a standard deviation can be calculated pixelwise based on the residual deviations relative to the background intensity.

2. *Identification of events.* A systematic scan through the light curves of all pixels is performed in search of “significant” peaks, i.e. peaks larger than Σ_P above the background value (with $\Sigma_P = N \sigma_{ov}$, and $N \geq 2.5$). A peak is assumed to be of solar origin if this level of significance is reached in at least two subsequent images. This extra criterium avoids the accidental acceptance of some exceptionally large statistical fluctuation or the misidentification of an overlooked cosmic ray, since both artifacts are expected to produce a jump in emission in a single image only.
3. *Determination of event dimensions.* Once a peak in the light curve of an individual pixel has been identified as a so-

lar brightening, the extent of the event is estimated in the temporal and in the spatial directions. A brightening is defined as the space-time region surrounding the peak where the detected intensity exceeds consistently the background value at the Σ_E confidence level (with $\Sigma_E = N\sigma_{ov}$, and $N \geq 1.5$). All pixels in this space-time region are excluded from further analysis so that the same brightening cannot be detected again in a neighbouring pixel's light curve.

The detection scheme as it is described in the previous three steps has a potential drawback: some long-lasting brightenings will affect the calculated background value (estimated too high) and the corresponding standard deviation (also estimated too high). As a result, small events might be overlooked and space-time extents might be significantly underestimated. To avoid this problem, the above 3 steps are repeated iteratively. In each iteration, the background values and standard deviations are updated after excluding the pixels where a brightening was detected in previous iterations. The whole process is repeated until the global statistical properties of the detected events have converged to within a few percent. This typically happens within 2, or occasionally up to 4, iterations. Based on the space-time region surrounding the peak where the detected intensity exceeds consistently the background value at the Σ_E confidence level, we record for each event the following characteristics:

- *The duration* as the time-interval between the earliest and the latest pixel exceeding the Σ_E confidence level.
- *The size* as the maximal area that exceeds the Σ_E confidence level during the lifetime of an event.
- *The peak intensity* that is reached by some pixel within the space-time region and the coordinates of that pixel in the field-of-view.
- *The radiative loss* as the integral over the whole space-time region of all the DN-values above background. We have converted this integrated emission to a radiative loss expressed in erg using a conversion factor of 5.3×10^{19} erg per DN recorded over 1 pixel in the Fe XII bandwidth and 2.0×10^{20} erg per DN recorded over 1 pixel in the He II bandwidth. These conversion factors are based on pre-flight calibrations of the EIT throughput with a self-consistent correction for the instrument aging (Moses et al. 1997). Taking account of the caveats discussed in Appendix A, we expect these numbers to be accurate by no more than a factor of 2, which is enough for the following applications.

4.2. Brightenings detected in the transition region

In table 4, we list the number of events found by applying this detection method with different values of the peak threshold Σ_P . As expected, the number of events rises tremendously when the threshold is decreased. Note that we express the peak threshold Σ_P in terms of the standard deviation σ_{ov} , based on the observed variability. This means that we are actually detecting peaks that exceed a very high level of significance in terms of the instrumental noise level (e.g. $2.5 \sigma_{ov} \approx 20 \sigma_{pn}$, see Fig. 2). Using more conventional threshold values (say $\Sigma_P = 2.5 - 5.0 \sigma_{pn}$)

Table 4. Number of events detected at a peak threshold Σ_P and with an edge threshold Σ_E . Only events which have their full duration within the sequence length and which are not adjacent to image edges are counted in the third column.

Σ_P	Σ_E	number of events detected	full Sun birthrate
$5 \sigma_{ov}$	$2 \sigma_{ov}$	188	0.3/s
$4 \sigma_{ov}$	$2 \sigma_{ov}$	1473	2.4/s
$3 \sigma_{ov}$	$2 \sigma_{ov}$	9187	14.4/s
$2.5 \sigma_{ov}$	$1.5 \sigma_{ov}$	13067	19.9/s

would result in the identification of virtually every fluctuation as a brightening, in agreement with our earlier assessment that 100 % of the transition region is fluctuating. So, as we cannot find an intrinsic low-amplitude cut-off for those brightenings, and as we are trying to identify and characterise individual events, it is reasonable to choose a threshold that is not dictated by the weak instrumental noise but instead reflects the fuzzy boundary between “resolved” and unresolved “transients”. In this scheme, it is legitimate to reject events with amplitudes below $3 \sigma_{ov}$, as σ_{ov} reflects the statistics of unresolved fluctuations.

The histogram (Fig. 13) of the detected peak intensities above background looks linear in the log/lin scaling at high intensities, suggesting an exponential distribution. A breakpoint is clearly seen at small peak values which is resulting of course from the applied threshold. The comparison of the curve for $\Sigma_P = 2.5 \sigma_{ov}$ with the curve for $\Sigma_P = 3 \sigma_{ov}$ indicates that essentially all large amplitude events are detected, while additional events are detected only in the low range. Extrapolating this trend to even lower Σ_P thresholds might yield roughly another 12000 events, which would correspond to a birthrate of around 40 events per second over the whole Sun. The peak intensities above background in Fig. 13 correspond to emission enhancement factors mainly in the range from 1.1 to 2.7. However no correlation was found between the peak intensity of an event and the local averaged background value. In all subsequent figures of this subsection, we have used the brightenings detected in the He II sequence with $\Sigma_P = 3 \sigma_{ov}$ and $\Sigma_E = 2 \sigma_{ov}$.

In Fig. 14, we show the histogram of the maximal spatial extent reached by the brightenings during their lifetimes. A power law distribution with an index of -2.7 ± 0.15 is found in the range from 40 to 400 Mm². For event areas below 20 Mm², the distribution bends over, which is probably due to the limited spatial resolution of the instrument (3.75 Mm x 3.75 Mm = 14 Mm²). No clear correlation was found between the peak intensity of an event and its area (correlation coefficient 0.46).

Fig. 15 shows that the durations of the brightenings range from 2 min, up to around 60 min. The lower limit is due to the requirement that a brightening must be present in at least two images while the higher limit is a consequence of the running average used to obtain the background sequence. This low pass filtering process produces a rejection of transients longer than

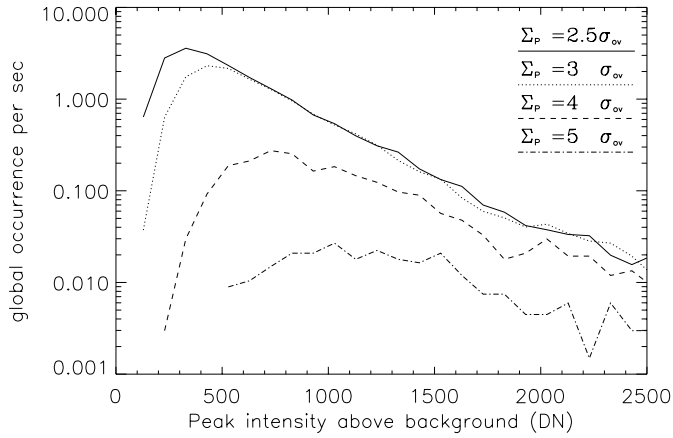


Fig. 13. Histogram (binsize 100 DN) of the peak intensity of the events detected in the He II transition region sequence.

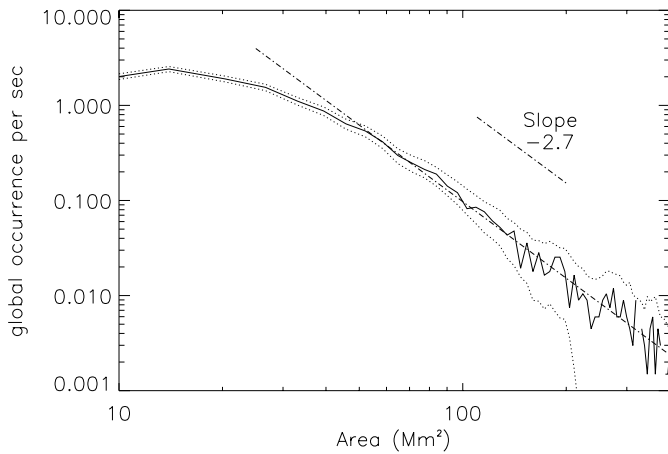


Fig. 14. Histogram (binsize 5 Mm²) of the maximal extent of the brightenings detected in the He II transition region sequence. The dotted lines are the 2.5 σ confidence levels based on Poisson statistics of the number of events in each bin.

1 hour. Below this critical time-scale, the distribution of events is unaffected, and above it, only very few events occur. Our conclusions are thus largely independent of the choice of the background separation method. For longer durations, the histogram tends to a power law distribution with an index of -3.1 ± 0.1 . For durations below 10 min, the distribution levels out. The duration of an event seems to be linearly correlated with its size (Fig. 16). The vertical stripes in the scatterplot are due to the discrete sampling in time of the images, while the horizontal stripes (less visible) correspond to our pixel sizes of 1.27 Mm². No clear correlation was found between the duration of an event and its peak intensity (correlation coefficient 0.41), although no brightenings seem to occur which combine a long duration with a small peak intensity. This vague trend causes the average durations to increase from 9 min for the events detected with the $\Sigma_P = 3 \sigma_{ov}$ threshold, up to 19 min for events detected with the $\Sigma_P = 5 \sigma_{ov}$ threshold.

Histogram (Fig. 17) shows that the radiative losses of the brightenings in the He II sequence range from somewhat below

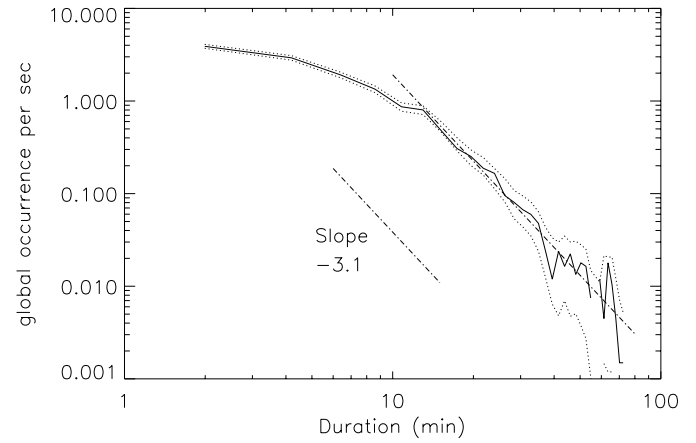


Fig. 15. Histogram (binsize = 132 sec) of the durations of the brightenings detected in the He II transition region sequence. The dotted lines are the 2.5 σ confidence levels based on Poisson statistics of the number of events in each bin.

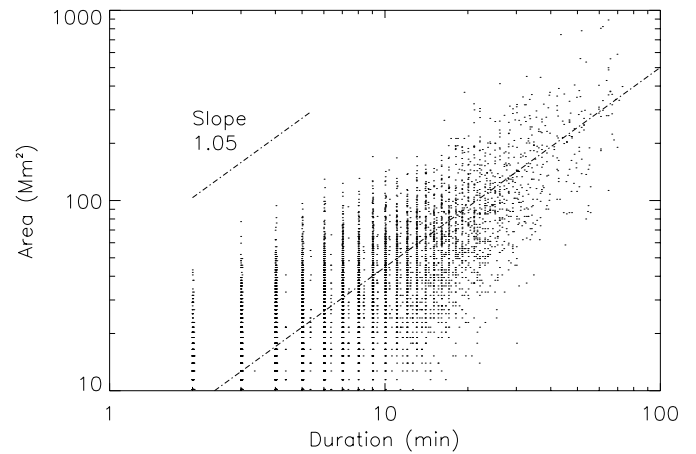


Fig. 16. Scatterplot of the brightenings detected in the He II transition region sequence. The brightenings are sorted vertically by their size and horizontally by their duration. The uncertainty on the slope is of the order of 0.04; the correlation coefficient is equal to 0.74.

10^{25} erg up to 10^{27} erg, so energetically speaking they are in between nanoflares (10^{24} erg) and microflares (10^{27} erg). Hudson (1991) derived a critical value of -2 for the power law index of the *energy* distribution of microflares or nanoflares. Below this critical value, the smallest events contribute the largest part of the total energy injected over all events. A histogram (Fig. 17) of the *radiative losses* shows a clear power law distribution with an index of -1.9 ± 0.1 . So, assuming that the radiative loss of a brightening is proportional to its total energy content (see Appendix A), this result means that larger events are energetically more important than small events, although only marginally.

Summing up the radiative losses of all events detected in the He II sequence and rescaling this by the size of our field of view and the duration of our sequence, we arrive at an “average brightening radiative loss” of 1.1×10^4 erg/cm²/sec. This is much lower than the total radiative loss of the upper chromosphere and corona (together 4×10^5 erg/cm²/sec, Withbroe

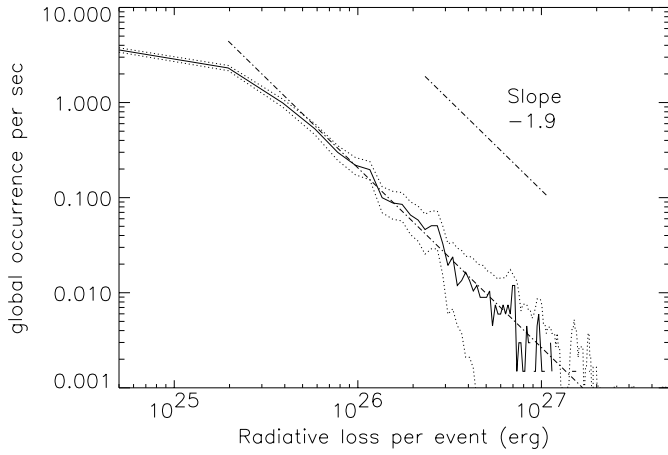


Fig. 17. Histogram (binsize= 3×10^{25} erg) of the radiative loss of the brightenings seen in the He II transition region sequence. The dotted lines are the 2.5σ confidence levels based on Poisson statistics of the number of events in each bin.

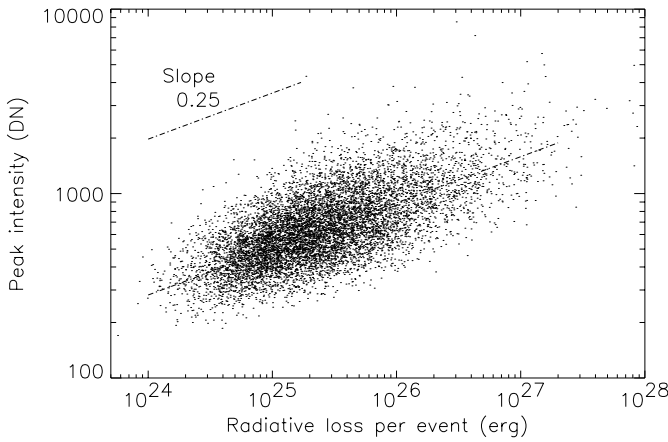


Fig. 18. Scatterplot of the brightenings detected in the He II transition region sequence. The brightenings are sorted vertically by their peak intensity and horizontally by their radiative loss. The uncertainty on the slope is of the order of 0.04; the correlation coefficient is equal to 0.66.

& Noyes 1977). It seems therefore unlikely that the brightenings have a direct relevance for the heating of the solar corona, though it cannot be ruled out that the brightenings are only the most visible aspect of an energetically more significant process. In addition, the power law index of Fig. 17 (-1.9) and its limited accuracy (± 0.1), leave open the possibility that a lot of energy is hidden in small, unresolved events that were not detected at the $\Sigma_P = 3 \sigma_{ov}$ level. The fact that 100 % of the pixels in the He II sequence are significantly variable (Fig. 2a and b), shows clear evidence that such events might be present.

For long lasting events, the duration of the event scales as the square root of its radiative output (Fig. 20). Again, the horizontal stripes in (Fig. 20) are due to the discrete sampling in time of the images. If we interpret the radiative output of an event as a measure of its energy content, then this result coincides with the correlation reported from numerical simulations of nanoflares (Dmitruk & Gómez 1997, and references therein).

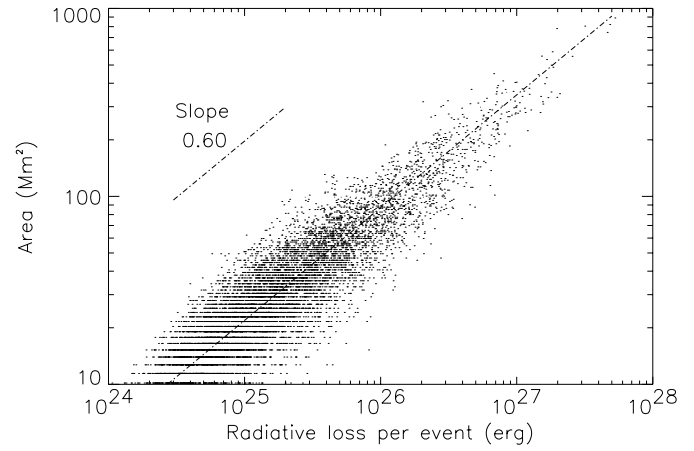


Fig. 19. Scatterplot of the brightenings detected in the He II transition region sequence. The brightenings are sorted vertically by their size and horizontally by their radiative loss. The uncertainty on the slope is of the order of 0.04; the correlation coefficient is equal to 0.90.

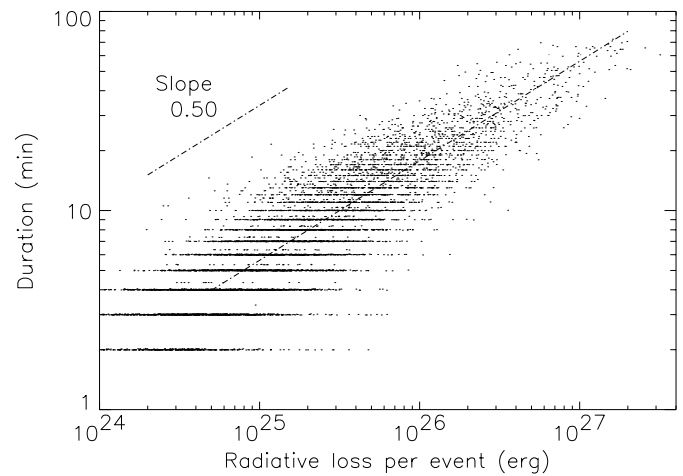


Fig. 20. Scatterplot of the brightenings detected in the He II transition region sequence. The brightenings are sorted vertically by their duration and horizontally by their radiative loss. The uncertainty on the slope is of the order of 0.04; the correlation coefficient is equal to 0.87.

This correspondence can be seen as indirect evidence that the transition region brightenings are related to nanoflare activity. Similarly, the peak intensity of the events scale approximately as the fourth root of the radiative loss (Fig. 18). The size versus radiative loss scatterplot (Fig. 19) shows a steeper correlation as compared to Fig. 20, coming close to a power $2/3$. In that case, the data would be consistent with a picture where the energy scales with volume.

In a recent paper, Harrison (1997b) reports on a class of quiet Sun brightenings that he calls “blinkers” which were observed with CDS in the transition region line O IV formed at slightly higher temperatures. The eleven blinker events which Harrison (1997b) observed have durations between 5 and 30 minutes (average 13 min), sizes from 22 to 44 Mm^2 and a thermal energy content of the order of 4.4×10^{25} erg. It was also established that blinkers do not have large (of the order of 100 km/s) line

of sight velocities. Later observations (Harrison 1997c) in the lines O III, O IV and O V brought the total number of blinkers observed by CDS up to around 100. Comparing these numbers with our histograms, it is clear that many of our brightenings have characteristics that are completely compatible with those of blinkers. We thus not only confirm the existence of these blinkers, but in addition our results indicate that they belong to a larger class of quiet Sun EUV brightenings with a wider range of characteristics. The fact that the birth rate of Harrison's blinkers is only 11 s^{-1} over the whole solar surface might be a consequence of visual detection missing the faintest ones.

EUV explosive events are another type of transition region transients that have been observed previously (Brueckner & Bartoe 1983). The usually quoted characteristics (Dere et al. 1989) of explosive events such as duration (60 sec), length scale (1.6 Mm), and kinetic energy content (6×10^{22} erg) are smaller than the range of values for the brightening events discussed in this paper. Nevertheless, Innes et al. (1997) discusses a few individual explosive events with durations up to 4.5 min and estimated length scales of up to 4 Mm. The major difference between the EUV explosive events and our brightening events resides in the vastly larger occurrence rate of EUV explosive events (a full disk quiet Sun birth rate of 600/s). Part of this difference is due to easier detection of the explosive events by their Doppler-shifts rather than by an intensity enhancement (see Porter et al. 1984 for a discussion related to this). If the explosive events are just the low energy extension of the He II brightening distribution (Fig. 17), then their occurrence rate is within the projection of the -1.9 power law. However, the lack of blinker Doppler-shifts argues against association with explosive events.

Concerning the location of the events, Harrison (1997a) suggests that the number distributions of pixel intensities may be described by a Gaussian distribution plus a tail of network locations with enhanced emission corresponding to the sites of the blinker events. To check this, we have plotted in Fig. 21 a histogram of the average background intensity of all pixels (solid line) which indeed has the appearance of a Gaussian distribution plus a tail towards higher intensities. The dashed line shows the average background intensity of the pixels at which the peak of a brightening occurred. Contrary to Harrison's suggestion, this figure indicates that the brightenings occur everywhere, not only in the network, but also in the cell interiors.

4.3. Brightenings detected in the low corona

From the difference in variability between the transition region and the low corona (Fig. 2), we can expect that brightenings seen in the low corona have very different statistics than those seen in the transition region. Only 12 events are detected in the low corona at the $\Sigma_P = 4 \sigma_{ov}$ and none at the $\Sigma_P = 5 \sigma_{ov}$ significance level. Furthermore, since $\sigma_{ov} \approx \sigma_{pn}$ (Fig. 2), the Σ_P threshold for the coronal sequence is practically based on instrumental noise statistics. All the following results for the coronal sequences are obtained with a $\Sigma_P = 3 \sigma_{ov}$ and $\Sigma_E = 2 \sigma_{ov}$ detection level. This yielded 228 events, corresponding

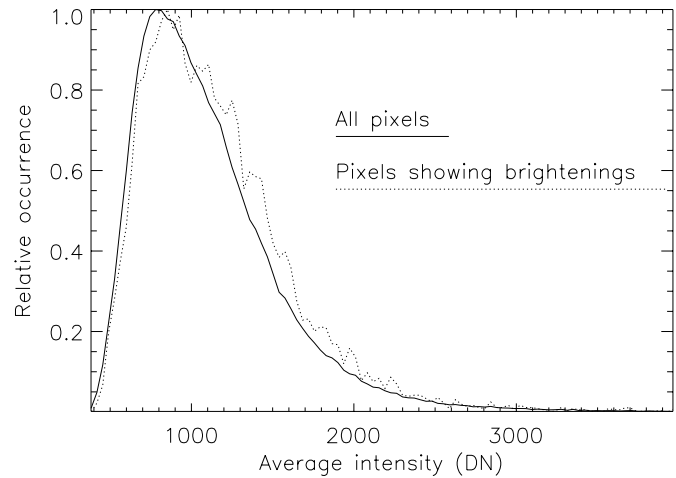


Fig. 21. A comparison of the distribution of the average background intensity of all pixels in the field of view, with the same distribution restricted to the pixels at which the peak of brightening occurred. Both histograms were rescaled to a maximum 1 and have a binsize of 35 DN.

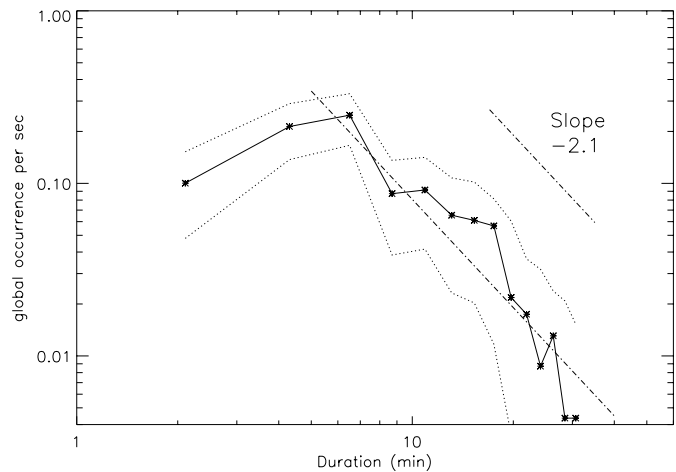


Fig. 22. Histogram of the durations (binsize 132 sec) of the brightenings seen in the Fe XII coronal sequence. The dotted lines are the 2.5σ confidence levels based on Poisson statistics of the number of events in each bin.

to a global birthrate of about 1.2/sec, for which the background intensity rose by a factor in the range from 1.1 to 2.3.

The histogram in Fig. 22 shows that the coronal brightenings have durations down to our detection limit (2 min) and up to about the running average window width (30 min) used for extracting the background. Due to the much lower number of events as compared to the transition region sequence, the confidence levels in the histograms span now a much larger region of uncertainty. Nevertheless, a powerlaw distribution can still be recognised with an index -2.1 ± 0.3 . The power law breaks sharply around durations of 5 to 6 min. No clear correlation was found between the duration of an event and its peak intensity (correlation coefficient 0.39).

The areas (Fig. 23) occupied by these events are typically tens of Mm^2 . Again a power law distribution provides a rea-

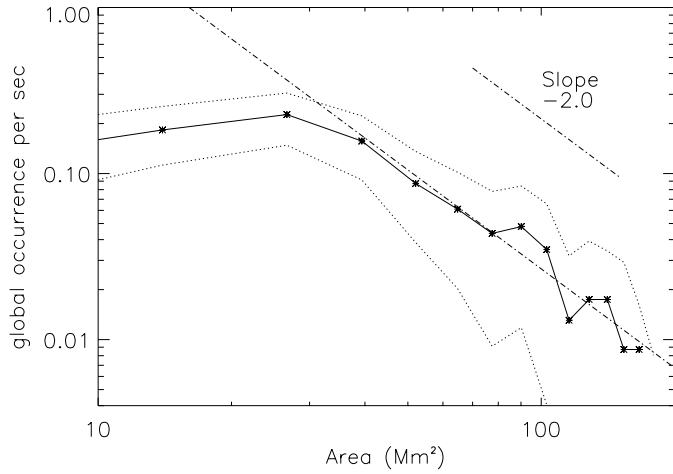


Fig. 23. Histogram of the area (binsize 14 Mm^2) of the brightenings observed in the Fe XII coronal sequence. The dotted lines are the 2.5σ confidence levels based on Poisson statistics of the number of events in each bin.

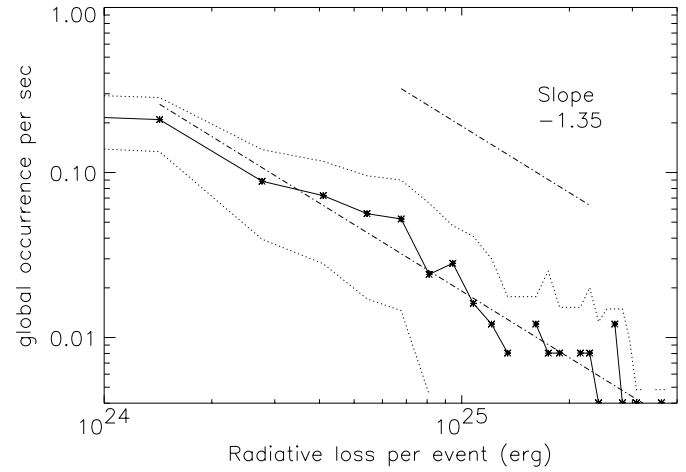


Fig. 25. Histogram (binsize= 2.4×10^{24}) of the radiative loss of the events observed in the Fe XII coronal sequence. The dotted lines are the 2.5σ confidence levels based on Poisson statistics of the number of events in each bin.

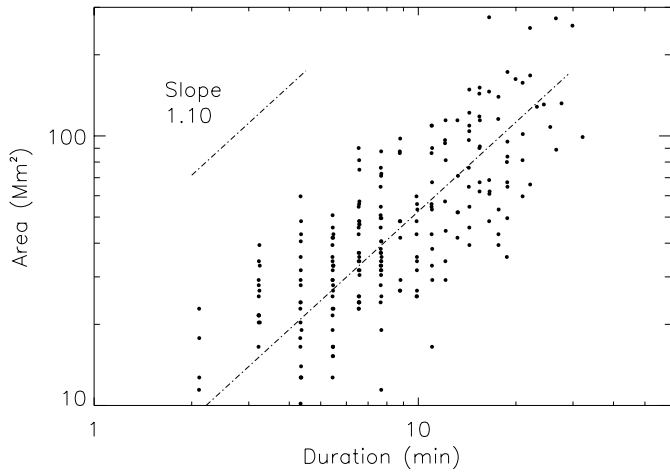


Fig. 24. Scatterplot of the brightenings detected in the Fe XII coronal sequence. The brightenings are sorted vertically by their duration and horizontally by their size. The uncertainty on the slope is of the order of 0.04; the correlation coefficient is equal to 0.75.

sonable fit for large areas with an index of (-2.0 ± 0.3) . Just as for the transition region brightenings, area and duration of an event are almost linearly correlated (Fig. 24) while no clear correlation can be found between the peak intensity and the area (correlation coefficient 0.34).

The radiative losses of the coronal brightenings are distributed between 10^{24} erg and 10^{26} erg and follow roughly a power law distribution with index -1.35 ± 0.2 . This is much lower than the corresponding power law of -1.9 for the transition region brightenings and also slightly lower than, but still compatible with, the -1.5 to -1.6 slope for active region transient brightenings found in SXT data by Shimizu (1995). As was the case for brightenings detected in the transition region, the duration of the coronal brightenings scales as the square root of the radiative loss (Fig. 28). The dependences of the peak intensity (Fig. 27, slope 0.30) and of the area (Fig. 26, slope 0.65) on the

radiative loss are slightly steeper for the coronal brightenings than for the transition region brightenings. However, since all the correlation slopes are given only with an accuracy of 0.04, this difference is not significant.

Since the radiative energy loss in Fig. 26 is proportional to the $3/2$ power of the area, the data are consistent with a picture where the energy scales with volume. With this assumption of constant energy density for all events, the mean energy density is $0.0125 \text{ erg cm}^{-3}$. Following this assumption, the emission measure calculated from these events implies a plasma density of $8.8 \times 10^8 \text{ cm}^{-3}$. For an unit volume of plasma of temperature $1.5 \times 10^6 \text{ K}$ at this density, the thermal energy density is 0.17 erg cm^{-3} . The difference in energy density could be due to the difference in the effective temperature of the observed plasma and the temperature sensitivity of the 195 \AA bandpass, a filling factor less than unity, energy losses by processes other than radiation, or even errors in the assumptions for computing the emission measure with a single bandpass measurement.

We speculate that the weak EUV brightenings are the low-energy counterparts of the soft-X ray network flares observed by Krucker et al. (1997b) using the SXT on board Yohkoh. The events seen by Krucker et al. (1997b) are brightenings in the quiet corona with a duration of roughly 10 minutes, a thermal energy content of roughly 10^{26} erg and a FWHM of 5 to 8 arcsec. The fourfold lower birth rate of the soft-X ray network flares (0.33/s around the globe) can be explained by assuming that most of the Fe XII brightenings observed by EIT correspond to weaker energy releases for which no plasma is heated beyond $2 \times 10^6 \text{ K}$ and that are thus undetectable in (higher-temperature) soft X-rays. Krucker et al. (1997a) report evidence that some of the brightenings in another EIT coronal sequence, which was taken together with simultaneous VLA observations, indeed correspond to miniature flares characterised by the early acceleration of energetic photons.

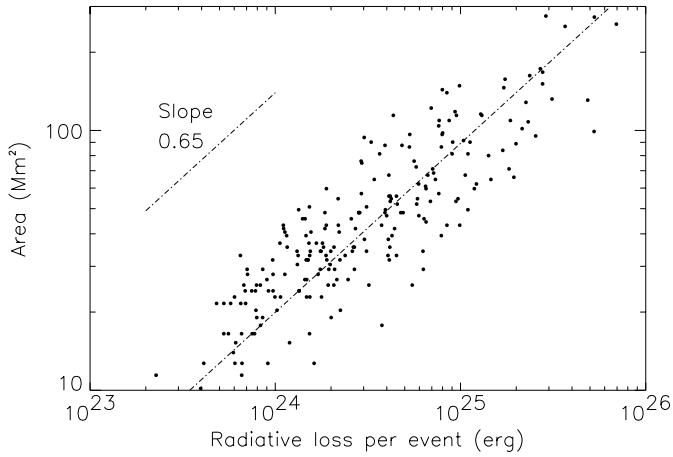


Fig. 26. Scatterplot of the brightenings detected in the Fe XII coronal sequence. The brightenings are sorted vertically by their size and horizontally by their radiative loss. The uncertainty on the slope is of the order of 0.04; the correlation coefficient is equal to 0.88.

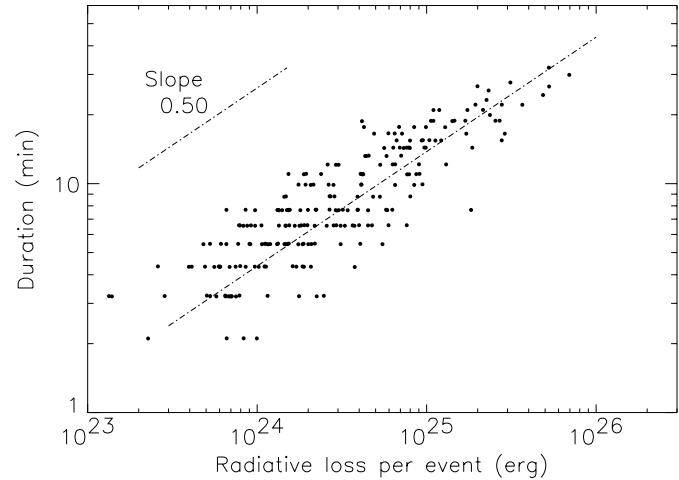


Fig. 28. Scatterplot of the duration of the brightenings seen in the Fe XII coronal sequence versus their radiative loss. The uncertainty on the slope is of the order of 0.04; the correlation coefficient is equal to 0.86.

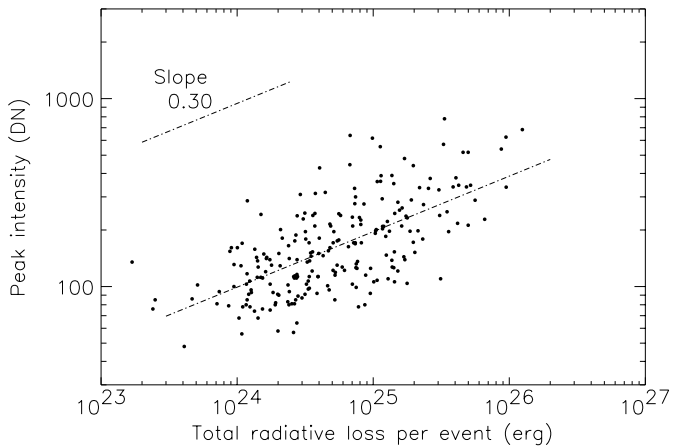


Fig. 27. Scatterplot of the peak intensity of the brightenings seen in the Fe XII coronal sequence versus their radiative loss. The uncertainty on the slope is of the order of 0.04; the correlation coefficient is equal to 0.65

5. Conclusions

Using two EIT image sequences of the quiet Sun, we were able to study the dynamics of the solar transition region and the low corona over a wide field of view. Two complementary approaches were followed to study these dynamics, namely: study of spatial and temporal properties and investigation of intermittent behaviour. By combining the relatively high-cadence (1 min) and the reasonable spatial resolution (3.75 Mm) with the wide field of view (600 Mm x 600 Mm) of this EIT data set, we are able to draw conclusions on the spatial distribution of the observed dynamics with high statistical accuracy. As such, this kind of sequence is especially well-suited to look for evidence of coronal heating mechanisms such as turbulence and microflaring.

5.1. Summary of observational results

As far as the Fe XII sequence is concerned, EIT has shown the quiet corona to be a turbulent plasma with an intricate texture of dim loops, some of which experience sudden emission enhancements. This conceptual view is supported by the following observational evidence:

- Although the large-scale appearance of the quiet corona is stable over 1 hour, small-scale temporal variability is distributed over the whole field of view in nontrivial patterns. Intrinsic solar variability can be confirmed in roughly 77 % of the pixels, while in the other pixels it may be masked by instrumental noise.
- The spatial omnidirectional spectrum has a power law index of -2.52 ± 0.05 , which is within the 2.5–2.6 range derived by Martens & Gómez (1992) from NIXT and YOHKOH/SXT observations of active regions. The existence of a power law spectrum not only supports the concept of a turbulent corona, but its specific value provides the first evidence that the same dynamical regime is found in both the cool plasma of the quiet corona and in the coronal active region loop systems.
- Analogously, the temporal power spectra follow a power law distribution, with an index of -1.85 ± 0.1 for the average spectrum over the whole field of view and a slightly steeper power law distribution (-2.0 ± 0.1) for the spectra of bright points and loops. Moreover, differential spectra of individual features showed discrete peaks at apparently random positions in the frequency range 0.5–4 mHz, which can be interpreted as a signature of intermittency.
- This intermittency was identified as brightenings of pre-existing loops and of bright points. We found several hundred of these events corresponding to a whole Sun birth rate of about 1.2/s. The histograms of the duration (several minutes), the size (tens of Mm^2) and the radiative loss (10^{24} – 10^{26} erg) of these events hint at power law distribu-

tions with indices of -2.1 ± 0.3 , -2.0 ± 0.3 and -1.35 ± 0.2 respectively.

It seems more difficult to extract a coherent picture from the He II transition region sequence. This is not completely unexpected, considering the small vertical extent of the transition region. As a result, we might be seeing distorted, indirect consequences of dynamics occurring above or below the transition region. In any case, the interpretation of our data should take into account the following observational facts:

- The transition region is even more dynamic than the low corona: in the transition region sequence, all pixels vary at a very high level of significance (the variability is on average twelve times larger than the expected instrumental noise). This difference in variability between the corona and the transition region is in agreement with previous results from Rabin & Dowdy (1992), Hansteen (1997) and Rüedi et al. (1997)
- The He II omnidirectional spatial spectrum (Fig. 5) cannot be fitted by a power law distribution. The observed departure from a power law at low wavenumbers might reflect the scale-distribution of the underlying energy source and suggests that a transition occurs around the supergranulation scale.
- In contrast, the temporal power spectra follow a power law distribution, providing evidence for a turbulent energy cascade. The power law index of -1.50 ± 0.1 is exactly in agreement with the $-3/2$ index derived by Kraichan (1965) for an MHD turbulent spectrum. This means that frequencies in the range of 0.1–7.5 mHz fall within the inertial range of MHD turbulence.
- In comparison with the Fe XII coronal sequence, we again find localised brightenings, though with a much higher birth rate (20–40/s around the globe) both in the network as in cell interiors. Also, the power law distributions found for the transition region brightenings (size: -2.7 ± 0.15 , duration: -3.1 ± 0.1 and radiative loss: -1.9 ± 0.1) are clearly different from the brightenings detected in the coronal sequence.

Despite all these differences between the brightenings detected in the Fe XII coronal emission and those in the He II transition region line, a remarkable similarity is discovered when comparing the relation between the different parameters that characterise a brightening. Versus the radiative loss, the area of a brightening scales with a power of 0.60–0.65, the peak intensity scales with a power of 0.25–0.30 and the duration scales with a power of 0.50–0.50; where each time, the first number refers to the brightenings detected in the He II transition region sequence and the second number to the Fe XII sequence. Since the uncertainty on all these numbers is of the order of 0.04, these pairs of indices are virtually identical. In addition, we found in both sequences that the peak intensity of a brightening is independent from its size and its duration.

5.2. Identification of the brightenings and implications for coronal heating

By comparing the characteristics of the brightenings detected by EIT in the quiet corona with those of previously reported transients, we identified the Fe XII brightenings as the low-energy counterpart of X-ray network flares observed by Krucker et al. (1997b) using the SXT on board Yohkoh. The lower energy content and the fourfold higher birthrate that we find, as compared to the X-ray network flare, are both consistent with the hypothesis that most of the Fe XII brightenings detected by EIT, correspond to weaker energy releases for which no plasma is heated beyond $2 \times 10^6 K$ and that are thus undetectable in (higher-temperature) soft X-rays.

Many of the brightenings which we detected in the transition region sequence have characteristics that are completely compatible with the characteristics of the “blinkers” that Harrison (1997b) detected in CDS data. We have thus not only confirmed the existence of these blinkers, but in addition our results indicate that they belong to a larger class of quiet Sun EUV brightenings with wider distributions of characteristics all of which follow power laws. We also compared the smallest brightenings that we detected in the transition region with EUV explosive events (Dere et al. 1989). If the explosive events are just the low energy extension of the He II brightening distribution (Fig. 17), then their much higher occurrence rate is within the projection of the -1.9 power law. However, the lack of large Doppler-shifts accompanying blinkers, argues against association with explosive events.

A remarkable similarity was discovered when comparing between both sequences the relation of the different parameters (size, duration, peak intensity and radiative loss) that characterise a brightening. This similarity suggests that both populations of transients might originate from the same physical process. The difference in the occurrence rate distributions of their parameters might be due to varying external circumstances in the corona as compared to the transition region. If we interpret the radiative output of an event as a measure of its energy content, then the square root relation of the duration of brightening to its radiative energy coincides with the correlation reported from numerical simulations of nanoflares (Dmitruk & Gómez 1997). This agreement can be seen as indirect evidence that both the coronal and the transition region brightenings are related to micro/nanoflare activity.

Following this line of reasoning, we had a closer look at the appearance of individual transition region brightenings. Although a study of the morphology of the brightenings is beyond the scope of the present paper, we can say that many of the brightenings in the transition region do not occur at a single location, but instead as a double (or occasionally multiple) brightening source. One of the sources is more intense. Some of the secondary brightenings start together with the primary brightening or after some delay. All these characteristics suggest that we are observing the footpoints of a small-scale loop and that chromospheric material is heated in response to the same event occurring somewhere along the loop. Many of the

brightenings observed in the He II line show an expansion of the enhanced source that follows the rise and fall of the intensity. If we assume that this is a genuine horizontal expansion of the heated plasma, this phenomenon can be interpreted as the rise at constant density of the heated plasma inside the diverging, expanding magnetic field at the height of the transition region. In this scenario, the fact that the plasma is allowed to expand while heated limits the rise in temperature and might explain why few brightenings are found at coronal temperatures.

A confirmation that the brightenings are indeed (side-effects of) reconnections events of low-lying quiet Sun loops would support the concept of the “magnetic carpet”. Schrijver et al (1998) describe how the mixed-polarity character of the magnetic field distribution of the quiet photosphere causes a multitude of loop lengths for loops connecting concentrations along the network, across cell interiors, and arching up to cross cells over a range of distances. Rapid emergence of ephemeral regions or small bipoles leads to a new view of the photospheric driving input for coronal heating mechanisms: whenever flux from a newly emerged small bipole cancels against existing flux of opposite polarity, part of the flux of that opposite polarity is in effect moved to the location of the other pole of the dipole. The canceled flux then, has been replaced by the surviving opposite polarity flux at another location. For long connections, these footpoint reconnections lead to an effective braiding of the fieldlines, because the footpoint is moved over a distance small compared to the loop length. Moreover, the impulsive-like character of these reconnections might yield enough high-frequency input to drive wave-heating mechanisms.

Acknowledgements. The authors would like to thank Drs. J. Cook, K. Dere, J. Newmark, Y.M. Wang, and K. Waljeski. Moreover, it is a pleasure to acknowledge the EIT science planner and the EOF staff, for implementing these non-standard sequences, and the whole EIT Consortium for making the instrument a reality. SOHO is a project of international cooperation between ESA and NASA. This work was supported by the Belgian Federal Services of Scientific, Technical and Cultural Affairs (SSTC/DWTC). D. Moses was supported by the Office of Naval Research and NASA grants NDPRS-86759E and NDPRA-09930F.

Appendix A: calculation of radiative losses

In order to obtain an estimate of the energy involved in the observed EUV brightenings, we have calculated the radiative energy losses for each of the brightenings. The calculation of the radiative energy losses from narrow-band (but not single line) EUV intensities requires a set of assumptions about densities, abundances, and temperatures in the observed plasma. Interpretation of the radiative energy loss as a measure of the total energy released in a heating event involves a second set of assumptions. Conduction is potentially a substantial energy loss mechanism in the corona. Although a consistent treatment of conduction losses in the corona has not been completed, it is common to assume that the conductive losses are approximately equal to the radiative losses in the corona. The large temperature gradients observed in the transition region provide evidence that

conduction is not a significant process in the transition region. Even if the assumptions break down for some particular case, the following analysis is useful simply as a study of the intensity variations observed in the respective EUV bandpasses.

The radiative energy losses are obtained from the product of the radiative loss function of Cook et al. (1989) and an emission measure derived from the EUV intensity. To obtain an emission measure, a synthetic spectrum is calculated by assuming a density and temperature using the ISOTHERMAL routine (Newmark 1996) of the CHIANTI spectroscopy data base (Dere et al. 1997). The synthetic spectrum is folded into the instrument parameters of the relevant EIT sector to obtain the count rate observed by EIT for a unit emission measure. The instrument calibration used for this calculation is a modification of the instrument parameters presented in Delaboudinière et al (1995) with the filter throughputs of Song (1995). Further work on the SOHO EIT calibration is in progress with the data obtained from the EIT Calibration Sounding Rocket.

The densities assumed in the synthetic spectrum calculation are $1.5 \times 10^9 \text{ cm}^{-3}$ for the corona (Fe XII) and $1.0 \times 10^{10} \text{ cm}^{-3}$ for the transition region (He II). Since the EIT bandpasses are dominated by resonance lines, the spectra are relatively insensitive to the input densities. The temperatures assumed are the temperatures of maximum ionization fraction for the dominant ion in each bandpass: $1.5 \times 10^6 \text{ K}$ for Fe XII and $5.0 \times 10^4 \text{ K}$ for He II. The contribution of lines formed at different temperatures within a given bandpass will be underestimated in this approach if the true differential emission measure is not strongly peaked at the assumed temperature. Such a contribution is minimal in the He II and Fe XII bandpasses for quiet Sun plasma. With the isothermal assumption, one makes an overall underestimate of the energy of an event.

For some of the transition region lines, including He II 304 Å, the differential emission measure, falls outside the trends set by the majority of transition region lines. The variation from this trend in differential emission measure can approach an order of magnitude. Thus, although the uncertainty of the emission measure calculation is on the order of a factor of two, there remains a caveat that should be kept in mind when interpreting our results. This caveat cannot be resolved with EIT data alone. A SOHO “Joint Observation Program” with CDS and SUMER may provide a more complete picture of the energy release of the EUV brightenings in the transition region.

References

- Benz, A.O., Krucker, S., Acton, L.W., Bastian, T.S., 1997, A&A, 320, 993
- Brueckner, G.E., Bartoe, J.-D.F., 1983, ApJ, 272, 329
- Chou, D.-Y., LaBonte, B.J., Braun, D.C., Duvall, Jr., T.L., 1991, ApJ, 372, 314
- Cook, J.W., Cheng, C.-C., Jacobs, V.L., Antiochus, S.K., 1989, ApJ, 338, 1176.
- Deeming, T.J., 1975, Ap&SS, 36, 137
- Delaboudinière, J.-P. et al, 1995, Sol. Phys., 162, 291
- Dere, K.P., Bartoe, J.-D.F., Brueckner, G.E., 1989, Sol. Phys., 123, 41
- Dere, K.P., Landi, E., Mason, H.E., Monsignori Fossi, B.C., Young, P.R., 1997, A&A, 125, 149.

- Dmitruk, P. Gómez, D.O., 1997, ApJ Lett., 484, L83
- Einaudi, G., Velli, M., Politano, H., Pouquet, A., 1996, ApJ Lett., 457, L113
- Georgoulis, M., Velli, M., Einaudi, G., 1997, in Proc. of the 5th SOHO Workshop, Oslo, ESA SP-404, 401
- Gómez, D.O., 1990, Fund. Cosmic Physics, N° 14, 131
- Gómez, D.O., Ferro Fontan, C., 1988, Sol. Phys., 116, 33
- Gómez, D.O., Martens, P.C.H., Golub, L., 1993a, ApJ, 405, 767
- Gómez, D.O., Martens, P.C.H., Golub, L., 1993b, ApJ, 405, 773
- Grappin, R., Pouquet, A., Léorat, J., 1983, A&A, 126, 51
- Groth, E.J., 1975, ApJ Suppl., 286, 29, 289
- Hansteen V.H., 1997, in Proc. of the 5th SOHO Workshop, Oslo, June 1997, ESA SP-404, 45
- Harrison, R.A., 1997a, in Proc. of the 5th SOHO Workshop, Oslo, June 1997, ESA SP-404, 7
- Harrison, R.A., 1997b, Sol. Phys., 175 (part 2), 467
- Harrison, R.A., 1997c, *private comm.*
- Heyvaerts, J., Priest, E.R., 1992, ApJ, 390, 297
- Hollweg, J.V., 1983, in M. Neugebauer (ed.), *Solar Wind V*, NASA Conf. Publ. 2280, p.5
- Hudson, H.S. 1991, Sol. Phys., 133, 357
- Innes, D.E., Inhester, B., Axford, W.I., Whilhelm, K., Nat, 386, 24, 811
- Kolmogorov, A.N., 1941, C. R. Dokl. Acad. Sci. SSSR, 30, 301
- Kraichnan, R.H., 1965, Phys. Fluids, Vol. 8, N° 7, 1385
- Krucker, S., Benz, A.O., Delaboudinière, J.-P., 1997a, in Proc. 5th SOHO Workshop, ESA SP-404, 465.
- Krucker, S., Benz, A.O., Bastian, T.S., Acton, L.W., 1997b, ApJ, 488, 499
- Landau, L., Lifchitz, E., 1971, *Mécanique des fluides*, Editions de Moscou.
- Martens, P.H.C., Gómez, D.O., 1992, PASJ, 44, L187
- Moses, D. et al, 1994, ApJ, 430, 913
- Moses, D. et al, 1997, Sol. Phys., 175, 571
- Newmark, J. 1996, EOS 77 (46), F557
- Parker, E.N., 1979, *Cosmical magnetic fields* (Oxford: Clarendon Press), pp. 359-391
- Parker, E.N., 1988, ApJ, 330,474
- Parker, E.N., 1989, Sol. Phys., 121,271
- Parker, E.N., 1991, ApJ, 372,719
- Porter, J.G., Toomre, J., Gebbie, K.B., 1984, ApJ, 283, 879
- Porter, J.G., Moore, R.L., Reichmann, E.J., Engvold, O. Harvey, K.L., 1987, ApJ, 323, 380
- Porter, J.G., Fontenla, J.M., Simnett, G.M., 1995, ApJ, 438, 472
- Rabin, D., Dowdy, J.F., 1992, ApJ, 398,665
- Ruëdi, I., Brković, A., Solanki, S.K., Harrison, R., Fludra, A., Huber, M.C.E., Stenflo, J.O., Stucki, K., 1997, in Proc. 5th SOHO Workshop, ESA SP-404, 641
- Schrijver, C.J., Title, A.M., Harvey, K.L., Sheely, N.R. Jr., Wang, Y-M., van den Oord, G.H.J., Shine, R.A., Tarbell, T.D. Hurlburt, N.E., 1998, Nat, *submitted*
- Schuster, H.G., 1984, *Deterministic Chaos: An introduction*, Weinheim, Physik-Verlag.
- Shimizu, T., 1995, PASJ, 47, 251
- Shimizu, T., Tsuneta, S., 1997, ApJ, 486,1045
- Song, X, 1995, PhD thesis, University of Paris XI.
- van Ballegooijen, A., 1986, ApJ, 311, 1001
- Walsh, R.M., Ireland, J., Harrison, R.A., Priest, E.R., 1997, in Proc. 5th SOHO Workshop, ESA SP-404, 717.
- Withbroe, G.L, Noyes, R.W., 1977, ARA&A, 15, 363